

Highly Sensitive Skin-Mountable Strain Gauges Based Entirely on Elastomers

Nanshu Lu, Chi Lu, Shixuan Yang, and John Rogers*

Quantifying naturally occurring strains in soft materials, such as those of the human body, requires strain gauges with equal or greater mechanical compliance. This manuscript reports materials and mechanics approaches are reported for an all-elastomer strain measurement device with gauge factor as high as 29 and with Young's modulus that approaches that of the human epidermis. These systems use thin carbon-black-doped poly(dimethylsiloxane) (CB-PDMS) for the strain gauges due to its high resistivity and strong dependence on strain, and thick carbon-nanotube-doped PDMS (CNT-PDMS) for the interconnects due to its comparatively low resistivity and weak dependence on strain. Devices composed of molded, straight resistors of CB-PDMS joined by serpentine-shaped interconnects of CNT-PDMS, both in a matrix substrate of PDMS, have electrical responses that depend almost entirely on the strain in the CB-PDMS. Integrated structures of this type have Young's moduli of 244 kPa, which lies within the range of values for the human epidermis. Such sheets can be readily laminated on and form conformal contact to the human skin, with only modest mechanical constraints on natural motions. Strains measured in this mode on the wrist are between 11.2% and 22.6%.

$$GF = \frac{\Delta R/R_0}{\varepsilon} \quad (1)$$

The GF s for metallic foils are typically between 2 to 5,^[1] due mostly to changes in length and cross-sectional area. A simple formulation assuming constant resistivity and constant volume yields $R/R_0 = (L/L_0)^2$.^[2] Since $R/R_0 = 1 + \Delta R/R_0$ and $L/L_0 = 1 + \varepsilon$, when $\varepsilon \ll 1$, $\Delta R/R_0 \approx 2\varepsilon$, which corresponds to $GF = 2$. Compared to metallic foils, semiconductor devices can exhibit much larger GF due to piezoresistive effects. Here, the resistivity changes rapidly with strain due to the dependence of the bandgap on inter-atomic spacing.^[3–5] For example, the gauge factor of p-type [110] single crystalline silicon can be as high as 200.^[3,6,7] As a result, for precision measurements, semiconductor gauges, also called piezoresistors, are preferred over metal foils. These types of devices are widely used as “hard” sensors attached to stiff materials such as metals, concretes and high modulus plastics for

1. Introduction

Strain gauges are devices designed to attach to a target object for the purpose of measuring deformations in a precise manner. The most common type of gauge consists of a patterned metal foil on a flexible plastic backing that attaches to the object with a suitable adhesive, such as cyanoacrylate. Deformations in the object lead to deformations in the foil, thereby causing its electrical resistance to change. The fractional change in resistance, $\Delta R/R_0$, is related to the mechanical strain ε by the gauge factor (GF):

structural health monitoring or quantifying specimen deformation. Recent work shows that ultrathin sheets of single crystalline silicon, i.e., nanomembranes,^[8] can yield similar types of devices in flexible form on thin plastic substrates.^[9]

Studies of biomechanics, physiology, and kinesiology require devices that can conform to the curvilinear surfaces of biological tissues and also can accommodate the large deformations that are often associated with them. Ordinary strain gauges made out of silicon slabs are clearly unsuitable for such uses, but so are flexible devices (metal foils or silicon nanomembranes) due to their inability to wrap complex curved objects or to stretch (i.e. respond in a reversible manner to strains much larger than 1%). Electrogoniometers and electrotorsionometers made of metal wires can be mounted on human joints to measure, in a bending mode, motions such as human elbow rotation and ankle dorsiflexion, but they cannot map spatial distributions of strain and they also impose unacceptably large mechanical constraints for measuring motions of soft parts of the body, such as the skin.^[10,11] Mercury-in-rubber strain gauges^[12] represent one solution, suitable for monitoring blood flow and tissue swelling by local measurements of skin extension. The filling requirements in the fabrication of such devices, however, restrict their geometries and modes of use. For example, most devices provide only single measurement capabilities, in closed loop form for application around approximately cylindrical parts of the

Prof. N. Lu, S. Yang
Department of Aerospace Engineering
and Engineering Mechanics
Texas Materials Institute
University of Texas at Austin
Austin, TX 78712, USA

C. Lu, Prof. J. Rogers
Department of Materials Science and Engineering
Beckman Institute for Advanced Science and Technology and Frederick
Seitz Materials Research Laboratory
University of Illinois at Urbana-Champaign
Urbana, IL 61801 USA
E-mail: jrogers@uiuc.edu



DOI: 10.1002/adfm.201200498

body such as toes or legs.^[12] Other approaches include platinum (Pt)-based strain gauges for integration onto surfaces of objects such as contact lenses to record changes in the curvature of the cornea for the diagnosis of glaucoma.^[13] These and other efforts establish a trend in strain gauge development toward increasingly soft and deformable mechanics, for biointegrated applications. To monitor the surface strains of human skin due to joint motion, tissue swelling, wound healing, or even emotional expression, a sheet of skin-like, highly sensitive strain gauges that can be directly applied onto the tissue surface would be ideal. Such a system could conformally laminate onto the curvilinear surfaces of human body without any mechanical fixturing or adhesives, and with an ability to follow the natural motions of the tissue without delaminating or imposing any mechanical constraint, similar to recently described “epidermal” electronic systems.^[14]

Electrically conductive rubber (ECR) is a promising class of material for this purpose, due to its intrinsically low modulus, low density, elastic mechanics and its pronounced piezoresistivity.^[15,16] ECRs can be prepared by dispersing conductive fillers such as carbon black (CB), carbon nanotubes (CNT) or metallic nanoparticles into elastomers such as poly(dimethylsiloxane) (PDMS).^[16–18] Molding and curing processes can be used to manipulate such materials, which we refer to generally as conductive PDMS (CPDMS), into desired geometries for device integration.^[19–21] The electrical behaviors of CPDMS, such as the conductivity and the piezoresistance, depend strongly on filler concentration and morphology (e.g., particle size and structure) as well as filler–filler and filler–matrix interactions.^[16,22,23] With similar levels of loading, the sheet resistances of CB-doped PDMS (CB-PDMS) are several orders of magnitude higher than those of PDMS doped with multiwalled CNTs (CNT-PDMS).^[16,23] The piezoresistive effect is believed to arise from the different compressibilities between the filler and the matrix, such that the application of stress changes in the separations between individual filler elements.^[24–26] Applications of these effects range from tactile sensors^[21,27–29] to strain gauges^[15,30] and flow sensors.^[31] Examples of CPDMS-based soft strain gauges include knee-mounted electrogoniometers that use CNT-PDMS^[15] and “tattoo-like” epidermal strain gauges based on CB-PDMS.^[14] The former devices are attractive, in part, because they are capable of measuring deformations as large as 280%. Relatively low GF s (0.3) and requirements for bandages and/or adhesives to facilitate mounting on the human body^[15] present disadvantages. CB-PDMS gauges supported by polyimide and interconnected with serpentine metal wires can be integrated with thin (30 μm thick), low modulus elastomers (Ecoflex, Smooth-on, Inc.) to form devices that are exceptionally compliant, with mechanical properties approaching those of the skin itself. Arrays of such gauges, in the form of thin sheets, can spontaneously and reversibly laminate onto human skin, with the capability for quantifying and spatially mapping distributions of strain. A key drawback is that the overall GF (1.3) is compromised by the underlying stiff polyimide layer,^[14] which limits the magnitude of deformation in the CB-PDMS.

In this paper, we demonstrate the design, fabrication and characterization of high gauge factor, all-elastomer strain gauge systems, with Young's moduli within the range of the human epidermis. The devices combine CB-PDMS resistors, CNT-PDMS

conductors and an insulating PDMS matrix/substrate to yield, in mechanically optimized geometrical layouts, desired characteristics. Measurement of strains in human skin using sensor sheets of this type, physically laminated onto the wrist, illustrates a representative implementation. Here, the devices remain attached even under full-range bending of the joint, with minimal effects of mechanical constraint or mass loading.

2. Design and Fabrication

Design considerations include sample thickness and stiffness, as well as accuracy in strain sensing. To minimize the overall stiffness, materials for both the matrix and the electrically active components should have low Young's moduli (ideally, comparable to the skin itself) and an ability to accommodate large strain deformations (30% or more) with a linear, elastic response. Various features in the materials, mechanics and electrical transport properties are important. A typical device involves resistors (i.e., strain gauges) and conductors (i.e., electrical interconnect) connected in series, such that the change in resistance (ΔR) from an initial state (R_0) can be related, in a fractional sense, to the two individual components according to

$$\frac{\Delta R}{R_0} = \frac{(\Delta R_r + \Delta R_c)}{R_{r0} + R_{c0}} \quad (2)$$

where subscripts r and c denote resistor and conductor respectively. Applying Equation (1) to each ΔR , yields

$$\frac{\Delta R}{R_0} = \frac{(GF_r \varepsilon_r R_{r0} + GF_c \varepsilon_c R_{c0})}{R_{r0} + R_{c0}} \quad (3)$$

A goal in mechanics and materials design is to configure the system such that the overall resistance change approaches the local resistance change of the resistor, i.e.,

$$\frac{\Delta R}{R} \approx GF_r \varepsilon_r \quad (4)$$

This outcome can be achieved by minimizing R_{c0} , GF_c , and ε_c . Since CB-PDMS has a much higher sheet resistance than CNT-PDMS at similar filler loading fractions,^[16] we use the former material for the sensors and the latter for the conductors, to yield $R_{c0} \ll R_{r0}$. Minimization of GF_c , requires consideration of two factors: the intrinsic material properties and the structure of the device. The intrinsic gauge factor of CPDMS itself is controlled by the type of filler and its loading fraction. The gauge factor of a structure of CPDMS has contributions from both the material and the geometry. Inspired by the shapes for metal interconnects in stretchable electronics,^[32–35] we exploited CNT-PDMS conductors in serpentine layouts, to minimize both the effective GF_c and ε_c .

The fabrication procedures appear in **Figure 1**. We prepared two types of CPDMS by mixing 25 wt% carbon black (VULCAN XC72R, Carbot Corp.) in one case and 15 wt% multiwall carbon nanotubes (CheapTubes.com) in the other, both with 30:1 (base polymer: curing agent) PDMS (Sylgard 184 Silicone Elastomer, Dow Corning Corp.) using a drill mixer (DR260B, Black & Decker). Figure 1A shows a schematic illustration of the

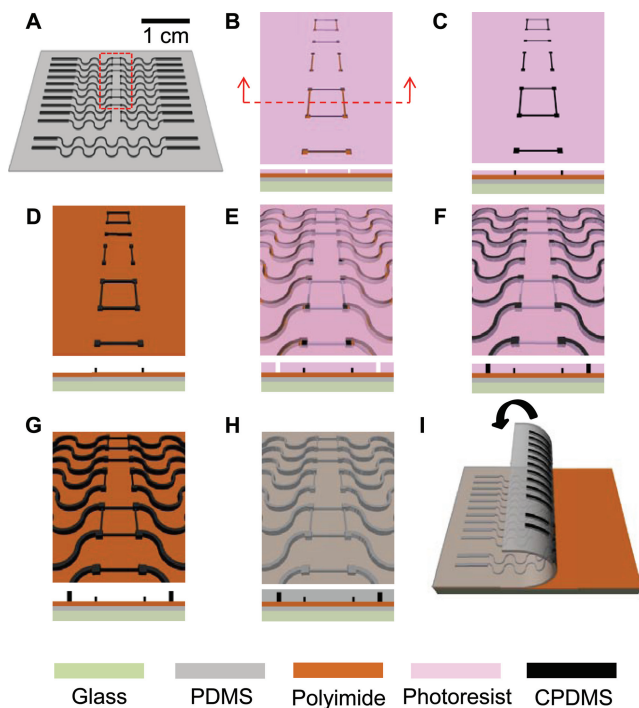


Figure 1. Schematic illustrations of fabrication procedures for all-elastomer strain gauges. A) Full-sized completed device. Tilted top views and cross-sectional views of the fabrication steps corresponding to the red dotted box in Frame A are provided in Frames B through H. B) Positive photoresist patterned in the form of trenches with layouts matching desired resistors and Wheatstone bridge geometries, on a film of polyimide. C) CB-PDMS squeezed into the trenches with excess removed by a razor blade. D) Photoresist rinsed off after curing the CB-PDMS. E) Thick layer of photoresist patterned in the form of trenches with layouts matching the interconnects. F) CNT-PDMS squeezed into the trenches with excess removed by a razor blade. G) Photoresist rinsed off after curing the CNT-PDMS. H) Cast PDMS to cover all of the patterned features. I) Peeling the entire integrated structure from the polyimide to yield a device shown in (A).

as-fabricated all-elastomer strain gauge, including both CPDMS components in a PDMS matrix. Magnified views corresponding to the fabrication steps for the area defined by the red dotted box are shown in Figure 1B–H. Laminating a sheet of polyimide (Kapton HN, DuPont) onto a glass substrate coated with a thin layer of PDMS cleaned by acetone and isopropanol (IPA) represents the first step. A positive photoresist (10 μm thick; AZ 4620P, AZ Electronic Materials Corp.) patterned with trenches defines the geometry of the sensing components, as shown in Figure 1B. Squeeze casting a mixture of uncured CB-PDMS into these trenches with a razor blade and then gently scraping off excess material, leaves the sample in the configuration shown in Figure 1C. Curing the CB-PDMS in a 70 °C oven for 2 h and then rinsing away the photoresist with acetone yields isolated features for the sensor components of the system, as shown in Figure 1D. Repeating steps B to D creates patterns of thick (20 μm) CNT-PDMS interconnects, as shown in Figure 1E–G. The final step involves uniformly casting 30:1 PDMS (0.3 mm thick) over the entire structure and then curing at 70 °C for 2 h as shown in Figure 1H. Since PDMS has weak adhesion to

polyimide, the integrated system can be peeled away easily, leaving all of the CPDMS structures embedded, as shown in Figure 1I. Ribbon cables, in the form of anisotropic conductive films (ACF, Elform Heat Seal Connectors), attached to ultra-violet ozone (UVO) treated CPDMS pads at the edges of the device, provide means for electrical measurement and evaluation on skin. Here, the cable terminates on a customized printed circuit board with soldered wires that interface to a digital multimeter (DMM, SMU2055, Signametrics Precision Instruments) for resistance or voltage measurement.

3. Results and Discussion

Figure 2A shows a photograph of an as-fabricated strain gauge composed of linear CB-PDMS resistors interconnected by serpentine CNT-PDMS conductors embedded in a transparent PDMS matrix. A deformed state (i.e., horizontal stretching to a strain of 150%) appears in Figure 2B. Uniaxial tensile tests (Instron) with *in situ* electrical measurement allow evaluation of the GF , as shown in Figure 1C. According to Equation (1), the slope of the $(R - R_0)/R_0 \sim \varepsilon$ curve determines the GF . The results are 29.1 and -4.9 for the longitudinal and transverse resistors, respectively. The negative GF is due to Poisson's effect, where lateral contraction occurs in conjunction with longitudinal elongation. Finite element models (FEM; ABAQUS CAE) for the strain fields reveal the underlying physics of deformation. Young's moduli obtained by uniaxial stress-strain curves (Figure 2D) serve as input parameters, along with the detailed geometries. The measurements indicate that the Young's moduli for the CNT-PDMS, CB-PDMS and PDMS are 445 kPa, 275 kPa and 145 kPa respectively. The relative values of CNT-PDMS and CB-PDMS are consistent with the Guth^[36] and Halpin–Tsai^[37] models, which predict that increasing the aspect ratio of the fillers increases the moduli. The effective modulus of the composite strain gauge sheet is 244 kPa, which lies within the range of values for the human epidermis, 140 to 600 kPa.^[38–40] The symmetric and uniaxial tensile boundary conditions for the FEM are illustrated in Figure 2E. A contour plot of ε_{xx} for the integrated system appears in Figure 2F, for the case of an applied strain of $\varepsilon_{\text{appl}} = 10\%$. By symmetry considerations, only the left half of the system was modeled. The results show that while most of the PDMS matrix and the linear resistor structures experience a uniform strain of 10%, the average strain in the interconnects is only around 7%, where only around 30% of the interconnects experience strains higher than 9%. This reduction results from the ability of the serpentine structures to undergo slight rigid body rotations to accommodate the applied stretch. Contour plots of longitudinal strain ε_{xx} and transverse strain ε_{yy} are plotted in Figure 2G (without showing the PDMS matrix).

Such behaviors, as well as the intrinsic differences between CNT-PDMS and CB-PDMS, can be observed in measurements on linear and serpentine CNT-PDMS with the same length, shown in Figure 3A, with comparisons to the results of Figure 2C. Figure 3B shows the change in resistance for the CNT-PDMS structures of Figure 3A, as a function of the applied tensile strain. The initial resistance of the CNT-PDMS conductor is 0.31 M Ω , which is ten times lower than that of a CB-PDMS

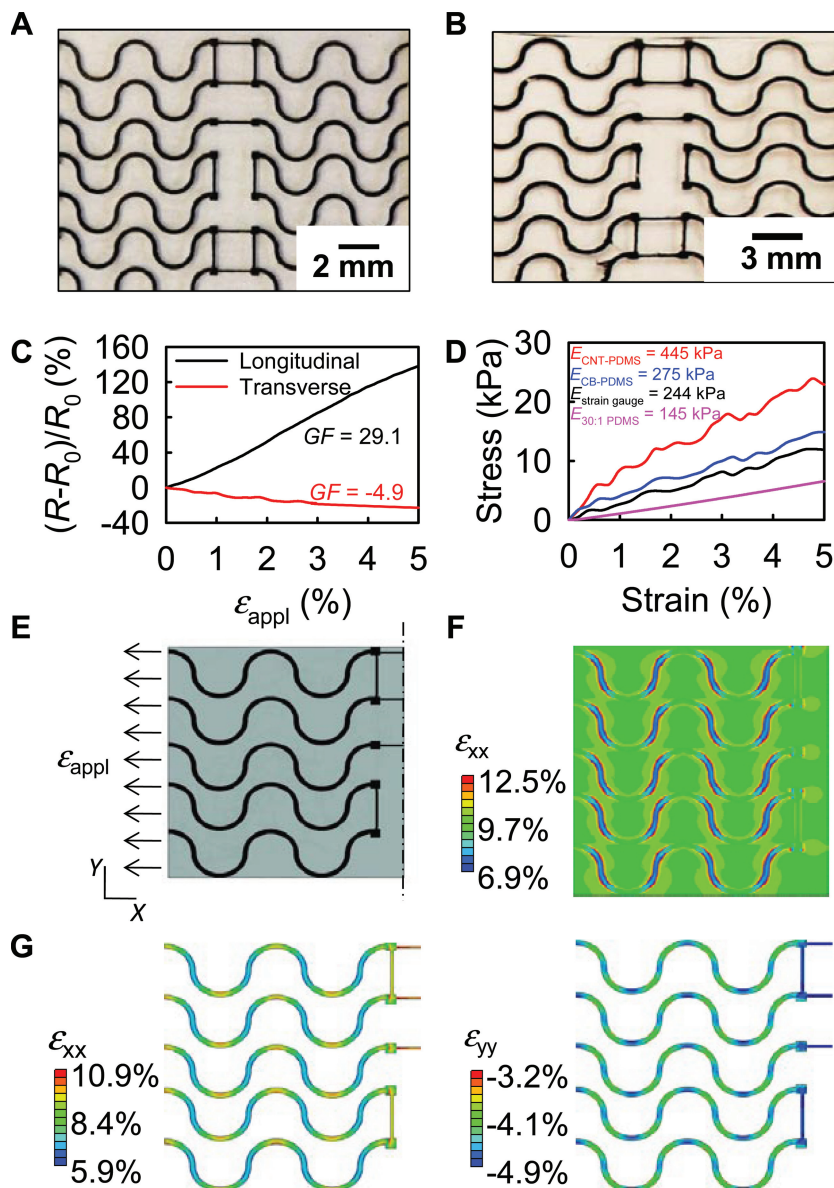


Figure 2. Tensile tests and finite element models (FEM) for all-elastomer strain gauges. A) Top view of an as-fabricated strain gauge. B) Top view of a strain gauge stretched by 150%. C) Change of resistance for longitudinal and transverse resistors as a function of tensile strain. D) Stress-strain curves and corresponding Young's moduli of the 30:1 PDMS matrix, CB-PDMS composite, CNT-PDMS composite and the strain gauge sample shown in Frame A.A). E) FEM model of the tensile test. F) Contour plot of the longitudinal strain in both the PDMS substrate and the CPDMS devices. G) Contour plot of the longitudinal strain in the CPDMS devices. H) Contour plot of the transverse strain in the CPDMS devices.

resistor with even shorter length and higher filler loading: 4.13 M Ω , qualitatively consistent with literature reports.^[16,23,41,42] The low percolation threshold and high conductivity in CNT-PDMS result from its unique filler geometry. Moreover, the GF for CNT-PDMS (0.52, as shown in Figure 3B) is significantly lower than that for CB-PDMS (29.1, as shown in Figure 2C). This is because when CB-PDMS is elongated, the conducting carbon particles can easily separate, resulting in breaking of conductive pathways and therefore, significant increases in

resistance. In contrast, CNTs may rotate and/or slide against each other to accommodate applied deformations. In this way, a significant fraction of the networks can remain connected and conductive, hence resulting in reduced changes in resistance.^[43] For these two reasons (i.e., low resistance and low GF), CNT-PDMS is more suitable than CB-PDMS as the interconnects; the opposite is the case for the sensors.

As highlighted by the FEM results, the GF not only depends on the materials, but also on the shape and associated mechanics of the conductor. For conductors of the same cross sectional dimensions and end-to-end lengths, the GF for strain applied along this length is twice as large for the linear case than it is for the serpentine structure, as illustrated in Figure 3B. The quantitative reason for this expected behavior is apparent from FEM shown in Figure 3C. Under the same level of deformation, the strain in the linear conductors is uniform and comparable to the applied strain; non-uniform strain appears in the serpentine case, with maximum values that are smaller than the applied strain. Since the system GF is defined as the resistance change per unit applied strain, the serpentine conductors have lower GF than linear ones.

A simple analytical model can capture this physics. Assume resistance is linearly proportional to length with a coefficient of β , and the gauge factor of a linear segment is GF_1 , which is measured to be 0.52 for CNT-PDMS (Figure 3B). The change of resistance of an infinitesimally short segment ds on an arbitrary curve, as shown in Figure 3D, is given by

$$d(\Delta R) = \beta ds \cdot GF_1 \cdot \frac{d(\Delta s)}{ds} \quad (5)$$

Since $R_0 = \beta L_0$, we can write,

$$\frac{d(\Delta R)}{R_0} = \frac{\beta GF_1 d(\Delta s)}{\beta L_0} \quad (6)$$

Integration of both sides over the total length of the curve yields

$$\frac{\Delta R}{R_0} = GF_1 \frac{\Delta L}{L_0} \quad (7)$$

which indicates the total change in resistance is proportional to the total change of the curve length. Since the serpentine shown in Figure 3A is formed by interconnected half circles, the fractional change of the total length of a half circle after uniaxial stretch of $\epsilon_{\text{appl}} = 10\%$ along the x axis (Figure 3E) can be given by

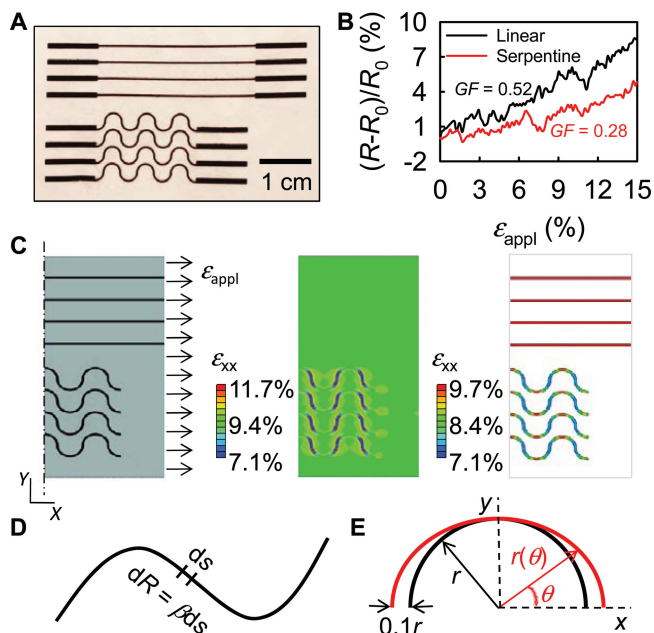


Figure 3. Comparison of linear and serpentine structures of CNT-PDMS. A) Top view of as-fabricated linear and serpentine structures of CNT-PDMS embedded in a PDMS substrate. B) Change in resistance of linear and serpentine structures of CNT-PDMS as a function of applied tensile strain. C) FEM model of the tensile test. D) Illustration of an infinitesimally short segment on an arbitrarily shaped curve, for analytical calculation. E) Illustration of a half circle stretched by 10% along the x axis, for analytical calculation.

$$\frac{\Delta L}{L_0} = \frac{\int_0^\pi r \sqrt{\sin^2 \theta + (1.1 \cos \theta)^2} d\theta - \pi r}{\pi r} = 0.051 \quad (8)$$

which is the same as the FEM output as shown in Figure 3C. The effective gauge factor of the serpentine conductor can then be obtained analytically as,

$$GF_e = \frac{GF_l \frac{\Delta L}{L_0}}{\varepsilon_{\text{appl}}} = \frac{0.52 \times 0.051}{0.1} = 0.27 \quad (9)$$

which is in excellent agreement with the measured value of 0.28, as shown in Figure 3B.

Strain gauges are responsive not only to tensile strains, but also to bending deformations and temperature changes. We performed experiments to explore these effects. Figure 4A presents a photograph of strain gauges wrapped around a cylindrical tube, as a representative setup for measuring the change of resistance as a function of the bending radius (black dots in Figure 4B). If we assume that the mechanical properties throughout the structure are approximately the same, then bending induced tensile strain along the outer surface of the structure is simply

$$\varepsilon = \frac{h}{2a} \quad (10)$$

where h is the sample thickness and a is the bending radius. The bending-induced change of resistance is, then,

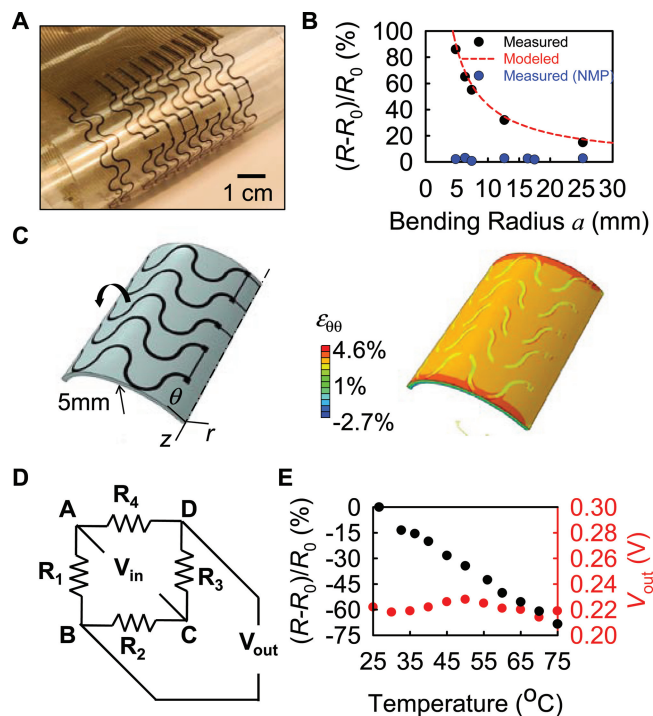


Figure 4. Calibration of bending and temperature effects of all-elastomer strain gauges. A) Bending tests conducting by wrapping devices around cylinders with different radii. B) Change in resistance as a function of bending radius. Black and blue dots are measured data for regular strain gauges and strain gauges placed along neutral mechanical plane respectively. The red dashed curve corresponds to an analytical model given by Equation (11). C) FEM of bending tests. The calculated strains match well with the analytical results. D) Schematic diagram of a Wheatstone bridge. E) Change of resistance of a resistor and change of output voltage of a Wheatstone bridge as functions of changes in temperature.

$$\frac{(R - R_0)}{R_0} = GF \frac{h}{2a} \quad (11)$$

Equation (11) is plotted as the red dashed curve in Figure 4B, which can properly capture the results of the bending experiment. Bending-induced strains are also verified through FEM as shown in Figure 4C. When a $h = 0.3$ mm sample is bent into a radius of $a = 5$ mm, Equation (11) gives a bending strain of 3%, which matches well with the FEM result in Figure 4C. To decouple bending-induced strain from tensile strain, we can intentionally place the CPDMS along a neutral mechanical plane by coating its surface with a layer of PDMS of identical thickness and stiffness with the underlying PDMS substrate. The change in resistance as a function of different bending radii for such a structure appears as blue dots in Figure 4B, which indicates negligible strain due to pure bending.

The effect of temperature can be explored both for an isolated resistor and a Wheatstone bridge configuration. The output voltage of a Wheatstone bridge (Figure 4D) is determined by

$$\frac{V_{\text{out}}}{V_{\text{in}}} = \frac{R_1}{R_1 + R_2} - \frac{R_4}{R_3 + R_4} \quad (12)$$

Changes in resistance of a resistor and the output voltage of a Wheatstone bridge appear as functions of temperature in

Figure 4E. Although the resistance of a single resistor decreases significantly with temperature, the output voltage from the Wheatstone bridge is insensitive to temperature changes because the resistance of each resistor changes in the same manner, such that the ratios (Equation 7) remain invariant. This compensation mechanism makes Wheatstone bridge configurations attractive for accurate and stable strain sensing.

For this reason, Wheatstone bridges serve as gauges for quantifying strains in human skin. Figure 5A plots the output voltage as a function of applied uniaxial tensile strain with an input voltage of 3 V. The change of output voltage is almost linear with strain. The output voltage as a function of

time under cyclic strain of up to 20% is plotted in Figure 5B. Although CPDMS resistance under constant strain or stress may drift due to creep or relaxation,^[46] this time-dependence behavior is often reduced after cyclic loadings and hence hysteresis can also be minimized.^[21] This type of elastomeric strain gauge sheet can be laminated onto the human wrist without fixtures or adhesives, as shown in Figure 5C. The high compliance and thin geometry of the system are essential in avoiding slippage or detachment from the skin as the wrist is bent (Figure 5C). These same properties minimize mechanical constraints on the natural motions of the skin, thereby ensuring that the measured strain reflects the actual deformation in skin. Corresponding measurements are provided in

Figure 5D. Voltage outputs from the Wheatstone bridge are fast and stable even under very quick repetitive motions. The variation in amplitude comes from the irregular bending of human wrist. According to the voltage-strain ratio given by Figure 5A and the amplitude in Figure 5D, bending induced strain on the skin surface is between 11.2% to 22.6%, which is in good correspondence with the human skin deformability.^[47] The reliability and repeatability of the gauges have been validated through hundreds of cyclic loadings. No signs of fatigue or degradation in either the device or the interface with the ribbon cables have been observed. The strain gauge can be easily peeled off the skin after the measurements without causing any redness or irritation. Since the gauge remains intact after the cyclic test, it can be reused, and integrated onto other regions of the skin surface.

4. Conclusion

In summary, all-elastomer, highly sensitive strain gauges can be fabricated by molding processes with two types of conducting elastomers, all integrated in a third, insulating elastomer. Demonstration experiments and calculations illuminate all of the key mechanics and materials aspects of these systems. Use on the human skin illustrates their operation. Particularly when integrated with stretchable electronics and other classes of sensors, these technologies have the potential to expand the range of function that can be achieved in biointegrated systems, with potential utility in wound monitoring, human-machine interfaces and others.

Acknowledgements

N.L. and C.L. contributed equally to this work. This material is based on work supported by

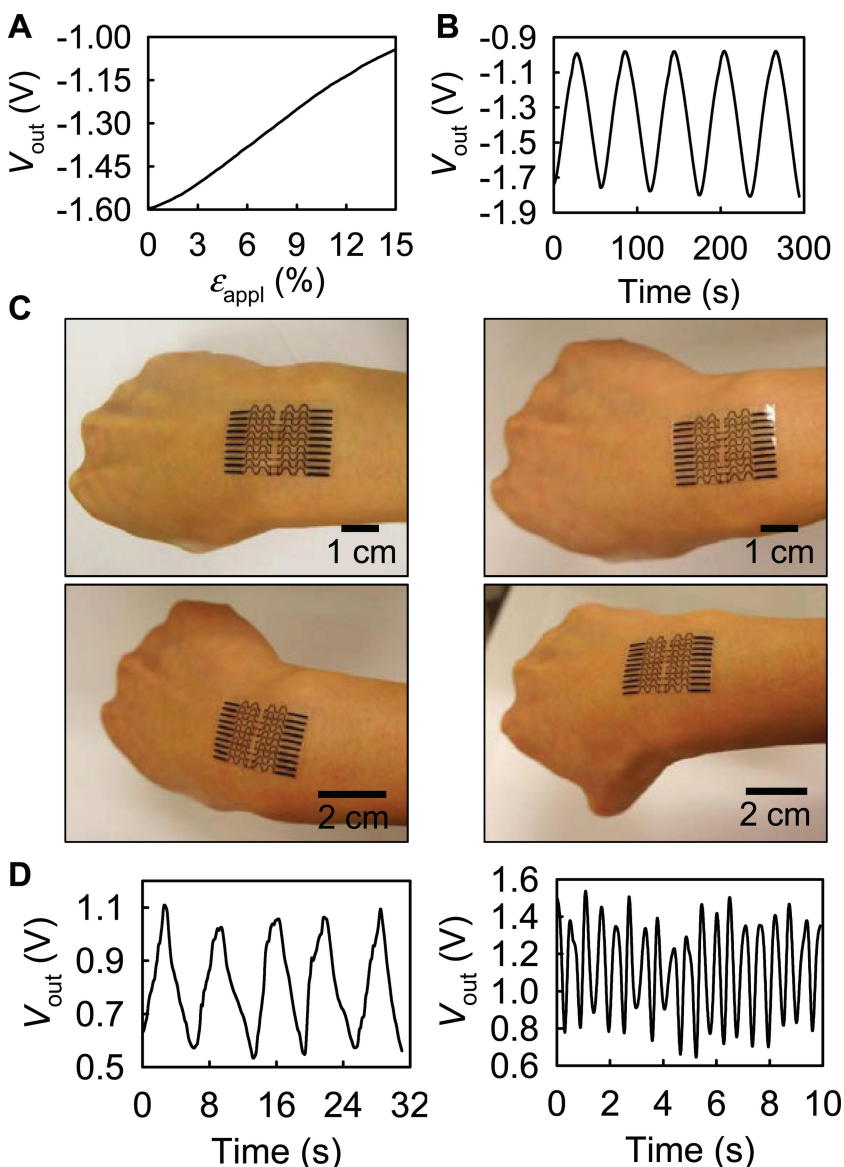


Figure 5. Application of all-elastomer strain gauges in Wheatstone bridge configurations to quantify strain associated with deformations in human skin. A) Output voltage as a function of uniaxial tensile strain. B) Output voltage under cyclic stretching with maximum strain up to 30%. C) Device laminated on the human wrist under various levels of bending. Output voltage when the wrist is undergoing D) slow and E) fast cyclic bending.

the a National Security Science and Engineering Faculty Fellowship and used facilities at the Materials Research Laboratory and Center for Microanalysis of Materials at the University of Illinois at Urbana-Champaign, supported by the U.S. Department of Energy, Division of Materials Sciences under awards DE-FG02-07ER46471 and DE-FG02-07ER46453. N.L. acknowledges support from a Beckman Postdoctoral Fellowship at the University of Illinois at Urbana Champaign and the startup fund provided by the Cockrell School of Engineering at the University of Texas at Austin.

Received: February 18, 2012

Revised: May 5, 2012

Published online: June 12, 2012

- [1] A. L. Window, *Strain gauge technology*, Elsevier Applied Science, London **1992**.
- [2] N. Lu, X. Wang, Z. Suo, J. Vlassak, *Appl. Phys. Lett.* **2007**, *91*, 221909.
- [3] C. S. Smith, *Phys. Rev.* **1954**, *94*, 42.
- [4] S. M. Sze, *Semiconductor Sensors*, Wiley, New York **1994**.
- [5] A. A. Barlian, W. Park, J. R. Mallon Jr., A. J. Rastegar, B. L. Pruitt, *Proc. IEEE* **2009**, *97*, 513.
- [6] Y. Kanda, *Sens. Actuators A* **1991**, *28*, 83.
- [7] S. Middlehoek, S. A. Audet, *Silicon Sensors*, Delft University Press, Delft, The Netherlands **1994**.
- [8] J. A. Rogers, M. G. Lagally, R. G. Nuzzo, *Nature* **2011**, *477*, 45.
- [9] S. M. Won, H.-s. Kim, N. Lu, D.-g. Kim, C. Del Solar, T. Duenas, A. Ameen, J. A. Rogers, *IEEE Trans. Electron Dev.* **2011**, *58*, 4074.
- [10] E. Chao, K. An, L. Askew, B. Morrey, *J. Biomech. Eng.-Trans. ASME* **1980**, *102*, 301.
- [11] K. Rome, F. Cowieson, *Foot Ankle Int.* **1996**, *17*, 28.
- [12] G. Bell, P. Nielsen, N. Lassen, B. Wolfson, *Cardiovasc. Res.* **1973**, *7*, 282.
- [13] M. Leonardi, E. M. Pitchon, A. Bertsch, P. Renaud, A. Mermoud, *Acta Ophthalmol.* **2009**, *87*, 433.
- [14] D. Kim, N. Lu, R. Ma, Y. Kim, R. Kim, S. Wang, J. Wu, S. M. Won, H. Tao, A. Islam, K. J. Yu, T. Kim, R. Chowdhury, M. Ying, L. Xu, M. Li, H. Chung, H. Keum, M. McCormick, P. Liu, Y. Zhang, F. G. Omenetto, Y. Huang, T. Coleman, J. A. Rogers, *Science* **2011**, *333*, 838.
- [15] T. Yamada, Y. Hayamizu, Y. Yamamoto, Y. Yomogida, A. Izadi-Najafabadi, D. N. Futaba, K. Hata, *Nat. Nanotechnol.* **2011**, *6*, 296.
- [16] C. Liu, *Adv. Mater.* **2007**, *19*, 3783.
- [17] S. R. Quake, A. Scherer, *Science* **2000**, *290*, 1536.
- [18] S. Rwei, F. Ku, K. Cheng, *Colloid Polym. Sci.* **2002**, *280*, 1110.
- [19] X. Niu, S. Peng, L. Liu, W. Wen, P. Sheng, *Adv. Mater.* **2007**, *19*, 2682.
- [20] K. S. Ryu, X. Wang, K. Shaikh, C. Liu, *J. Microelectromech. Sys.* **2004**, *13*, 568.
- [21] D. Kim, N. Lu, R. Ghaffari, Y. Kim, S. P. Lee, L. Xu, J. Wu, R. Kim, J. Song, Z. Liu, J. Viventi, B. de Graff, B. Elolampi, M. Mansour, M. J. Slepian, S. Hwang, J. D. Moss, S. Won, Y. Huang, B. Litt, J. A. Rogers, *Nat. Mater.* **2011**, *10*, 316.
- [22] A. Medali, *Rubber Chem. Technol.* **1986**, *59*, 432.
- [23] L. Bokobza, *Polymer* **2007**, *48*, 4907.
- [24] P. Pramanik, D. Khastgir, S. De, T. Saha, *J. Mater. Sci.* **1990**, *25*, 3848.
- [25] A. Celzard, E. McRae, C. Deleuze, M. Dufort, G. Furdin, J. Mareche, *Phys. Rev. B* **1996**, *53*, 6209.
- [26] M. Taya, W. Kim, K. Ono, *Mech. Mater.* **1998**, *28*, 53.
- [27] T. Someya, T. Sekitani, S. Iba, Y. Kato, H. Kawaguchi, T. Sakurai, *Proc. Natl. Acad. Sci. USA* **2004**, *101*, 9966.
- [28] K. Takei, T. Takahashi, J. C. Ho, H. Ko, A. G. Gillies, P. W. Leu, R. S. Fearing, A. Javey, *Nat. Mater.* **2010**, *9*, 821.
- [29] L. Chen, G. Chen, L. Lu, *Adv. Funct. Mater.* **2007**, *17*, 898.
- [30] C.-H. Cheng, L. Xiao, Y.-N. Cheung, C. Chao, M. Yang, K.-L. Kwok, P.-F. Chong, W. Leung, presented at *7th IEEE Conf. Nanotechnol.*, Hong Kong, China, August **2007**.
- [31] A. R. Aiyar, C. Song, S. Kim, M. G. Allen, *Smart Mater. Struct.* **2009**, *18*, 115002.
- [32] D. Gray, J. Tien, C. Chen, *Adv. Mater.* **2004**, *16*, 393.
- [33] T. Li, Z. G. Suo, S. P. Lacour, S. Wagner, *J. Mater. Res.* **2005**, *20*, 3274.
- [34] D. Kim, J. Song, W. M. Choi, H. Kim, R. Kim, Z. Liu, Y. Y. Huang, K. Hwang, Y. Zhang, J. A. Rogers, *Proc. Natl. Acad. Sci. USA* **2008**, *105*, 18675.
- [35] M. Gonzalez, F. Axisa, M. V. Bulcke, D. Brosteaux, B. Vandeveld, J. Vanfleteren, *Microelectron. Reliab.* **2008**, *48*, 825.
- [36] E. Guth, *J. Appl. Phys.* **1945**, *16*, 1707495.
- [37] J. Halpin, *J. Composite Mater.* **1969**, *3*, 732.
- [38] C. Pailler-Mattei, S. Bec, H. Zahouani, *Med. Eng. Phys.* **2008**, *30*, 599.
- [39] O. Kuwazuru, J. Saothong, N. Yoshikawa, *Med. Eng. Phys.* **2008**, *30*, 516.
- [40] M. Geerligts, L. van Breemen, G. Peters, P. Ackermans, F. Baaijens, C. Oomens, *J. Biomech.* **2011**, *44*, 1176.
- [41] L. Flandin, A. Chang, S. Nazarenko, A. Hiltner, E. Baer, *J. Appl. Polym. Sci.* **2000**, *76*, 894.
- [42] W. Thongruang, C. Balik, R. Spontak, *J. Polym. Sci. Pol. Phys.* **2002**, *40*, 1013.
- [43] T. Sekitani, Y. Noguchi, K. Hata, T. Fukushima, T. Aida, T. Someya, *Science* **2008**, *321*, 1468.
- [44] H. Chuang, S. Wereley, *J. Micromech. Microeng.* **2009**, *19*, 045010.
- [45] W. Shih, L. Tsao, C. Lee, M. Cheng, C. Chang, Y. Yang, K. Fan, *Sensors* **2010**, *10*, 3597.
- [46] M. Shimojo, A. Namiki, M. Ishikawa, R. Makino, K. Mabuchi, *IEEE Sens. J.* **2004**, *4*, 589.
- [47] V. Arumugam, M. Naresh, R. Sanjeevi, *J. Biosci.* **1994**, *19*, 307.